geosciences

MDPI

Article

High-Resolution Cyclostratigraphy Uncovers Variable Orbital Forcing in the Oligocene South China Sea

Yiyang Zhou [1,2], Enze Xu [3], Xijun Liu [1,*], Shangfeng Zhang [2,4] and Yaning Wang [2,4]

[1] School of Geosciences, Guilin University of Technology, Guilin 541000, China
[2] School of Geosciences, Yangtze University, Wuhan 430100, China
[3] China Southern Petroleum Exploration & Development Corporation, PetroChina, Haikou 570100, China
[4] Key Laboratory of Exploration Technologies for Oil and Gas Resources, Ministry of Education, Yangtze University, Wuhan 430100, China
* Correspondence: xijunliu@glut.edu.cn

Abstract

The Oligocene provides an important interval for examining climatic and sedimentary variability following the Eocene–Oligocene transition, but the expression of orbital forcing in low-latitude marginal seas remains incompletely understood. We integrate natural gamma-ray (GR) logging and microfossil records from Well L9 in the Pearl River Mouth Basin, northern South China Sea, to establish a cyclostratigraphic framework spanning approximately 34.6–21.7 Ma. A floating chronology based on 405 kyr cycle counting was anchored using an independently constrained Oligocene–Miocene boundary horizon. Spectral analyses identify approximately 405 kyr, 100 kyr, and 40 kyr components, together with longer-period variability near 2.4 Myr and 1.2 Myr. Amplitude-modulation analysis reveals an approximately 1.2 Myr component in the 40 kyr envelope, supporting an obliquity-related interpretation. In contrast, the 100 kyr envelope contains approximately 1.6 Myr variability rather than a clear 2.4 Myr component, leaving the eccentricity-modulation origin of the latter unresolved. Palynological evidence indicates generally cool and humid conditions during the early–middle Oligocene, followed by late Oligocene warming. Comparison with published climate records suggests correspondence with six recognized cooling episodes, although chronological uncertainty limits precise event alignment. These results provide a regional chronological and paleoenvironmental framework and highlight the need to distinguish observed long-period sedimentary variability from its proposed orbital origin.

Keywords: Milankovitch cycles; oligocene paleoclimate; cyclostratigraphy; astronomical time scale; South China sea; chronological framework; orbital origin; palynology

Check for updates

Academic Editors: Tadeusz Marek Peryt and Chunfang Cai

Received: 21 September 2026
Revised: 4 November 2026
Accepted: 9 November 2026
Published: 12 November 2026

Copyright: © 2026 by the authors. Licensee MDPI, Basel, Switzerland. This article is an open access article distributed under the terms and conditions of the Creative Commons Attribution (CC BY) license.

1. Introduction

The Oligocene offers an opportunity to examine climate-system behavior following the establishment of a major Antarctic ice sheet. Cooling across the Eocene–Oligocene transition (EOT) fundamentally altered the Cenozoic climatic background, but subsequent environmental change was neither uniform nor monotonic [1–4]. Existing reconstructions document substantial variability in temperature, ice volume, and ocean conditions, while important differences remain among records and interpretations [2,5–10]. Resolving this variability requires sedimentary archives that combine sufficient temporal coverage with independent chronological constraints. Such records can help evaluate how orbital variability was expressed in sedimentary systems under an evolving climatic background [11].

The northern South China Sea provides a useful setting for investigating orbital-scale environmental variability in a low-latitude marginal sea. Its sedimentary records integrate terrestrial material supplied from adjacent catchments with changes in shelf and ocean conditions [12–18]. Orbital influences may therefore reach the sedimentary archive through several pathways, including precipitation, runoff, sediment delivery, and changes in marine depositional conditions. These processes can modify the amplitude and timing of sedimentary responses, making it difficult to assign a unique climatic mechanism to an observed cycle. Integrating terrestrial and marine indicators provides a basis for evaluating the environmental significance of cyclic sedimentary variations.

Previous cyclostratigraphic studies have demonstrated that successions in the northern South China Sea preserve orbital-scale variability and can support improved astronomical chronologies [19,20]. In the Zhujiang Formation of the Baiyun Sag, natural gamma-ray records revealed prominent eccentricity-related cyclicity, particularly the approximately 405 kyr component [21]. Research on the Hanjiang Formation in the Lufeng Sag used spectral analysis and filtering to improve stratigraphic subdivision and correlation [22]. Studies of the Oligocene Lingshui Formation in the Changchang and Beijiao sags further developed astronomical frameworks and explored relationships among orbital variability, sedimentation, and paleoclimate [10,23]. These investigations demonstrate the value of well-log records for regional stratigraphic calibration and environmental reconstruction.

However, identifying a sedimentary period close to an astronomical period does not, by itself, establish its orbital origin. This distinction is particularly important for million-year-scale variability, for which a sedimentary succession may contain only a small number of cycles. Low-frequency spectral features can also be affected by detrending, age-model construction, and nonlinear climatic or depositional responses. In the lacustrine Funing Formation of the Subei Basin, Lin et al. (2026) [24] identified an approximately 173 kyr component in TOC but not in GR and proposed that sedimentary thresholds and nonlinear responses influenced its expression. This proxy-dependent cyclicity highlights the need to distinguish astronomical forcing from its sedimentary expression. Approximately 2.4 Myr and 1.2 Myr variability therefore requires evaluation beyond direct filtering, including examination of amplitude modulation in the corresponding shorter-period components. Comparing these envelopes with astronomical reference series can help distinguish plausible orbital associations from interpretations based solely on similarity in period.

The approximately 470-m-thick succession investigated in Well L9, Pearl River Mouth Basin, provides an opportunity to address these issues. The studied interval spans the latest Eocene to early Miocene and contains a high-resolution natural gamma-ray (GR) record together with palynological, calcareous nannofossil, and foraminiferal datasets. Available stratigraphic evidence does not indicate a major unconformity or structural repetition, although localized depositional interruptions cannot be excluded. Calcareous nannofossils and foraminifera provide chronological and marine environmental constraints, whereas palynological assemblages offer evidence for regional vegetation and climatic conditions. Their integration allows cyclic GR variability to be evaluated within a broader stratigraphic and paleoenvironmental framework.

This study aims to establish a chronological framework for Well L9 and evaluate the orbital and environmental significance of its sedimentary variability. The specific objectives are to: (1) construct a 405 kyr cycle-counted floating chronology and anchor it using independent stratigraphic constraints; (2) identify the principal cyclic components and assess the proposed origins of long-period variability through carrier-band amplitude-modulation analysis and comparison with the astronomical solution; and (3) integrate terrestrial and marine microfossil evidence to reconstruct regional paleoclimate and depositional changes and assess their correspondence with recognized cooling events.

2. Geological Background

The Pearl River Mouth Basin occupies the northern shelf and slope of the South China Sea, offshore from the Pearl River Delta (Figure 1). It extends between approximately 113°10′–118°00′ E and 18°30′–23°30′ N and covers about 177,000 km^2 [25,26]. Its Cenozoic architecture comprises fault-step zones, depressions, and intervening uplifts [27]. For the present study, the significance of this setting lies in the preservation of a thick shelf succession supplied by terrigenous sediment and affected by changes in accommodation. Regional investigations describe shelf and deltaic deposition during accumulation of the Zhuhai Formation, with substantial sediment delivery from the ancestral Pearl River system [28–30]. The studied interval therefore records the combined effects of sediment supply, basin evolution, and marine environmental change. The structural configuration of the Baiyun Depression and adjacent tectonic units, together with the location of Well L9, is shown in Figure S1.

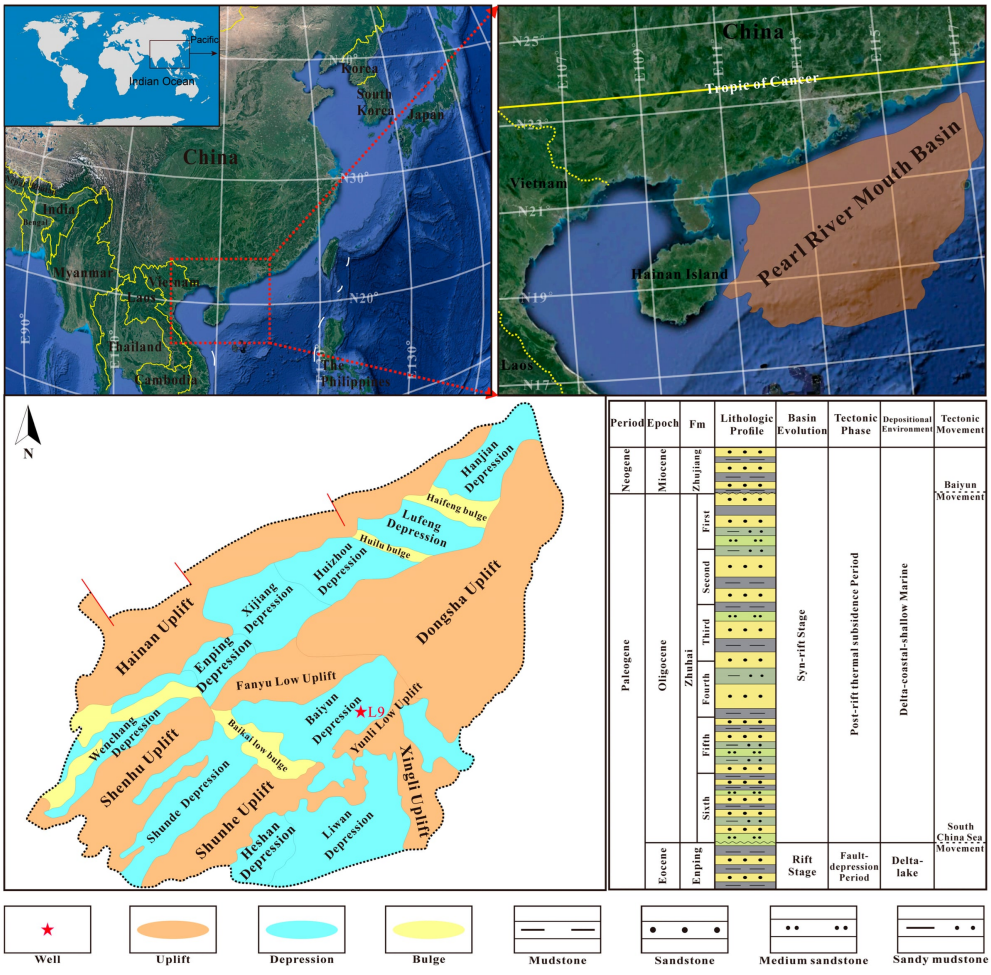


Figure 1. The structural units and stratigraphic filling evolution of the Pearl River Mouth Basin in the South China Sea.

The study covers 3156–3626 m in Well L9, a succession approximately 470 m thick extending from the upper Enping Formation to the basal Zhujiang Formation. The analyzed interval spans 3156–3626 m and was deposited in a shallow-marine shelf setting. It consists mainly of interbedded sandstone and mudstone. The mudstone is predominantly gray, with locally developed light-gray silty mudstone, whereas the sandstone is light gray to white and predominantly very fine- to fine-grained, with localized medium- to coarse-grained beds. The available well-log, biostratigraphic, and regional sequence-stratigraphic data do not indicate a

regional unconformity, large-scale stratigraphic omission, or structural repetition within the studied interval, providing a long-term stratigraphic framework for the present cyclostratigraphic study. This succession preserves abundant paleoclimate information, offering valuable insights into the paleoclimate evolution in the South China Sea region.

3. Data and Methods

3.1. Data Series Selection and Stratigraphic Assessment

Reliable cyclostratigraphic interpretation requires a stratigraphic assessment of potential discontinuities and a sufficiently resolved record of environmentally sensitive sedimentary variability [31–33]. The natural gamma-ray (GR) log from 3156–3626 m in Well L9 was selected because it provides continuous downhole measurements at a nominal spacing of 0.125 m, substantially finer than the sampling resolution of the microfossil datasets. In this siliciclastic succession, GR variability is interpreted primarily in relation to sediment composition and fine-grained terrigenous input, rather than as a direct measure of temperature [34,35]. Its climatic significance is therefore evaluated alongside lithological and paleontological evidence.

The sediments in the Pearl River Mouth Basin primarily originate from the Pearl River watershed and nearby mountainous regions [36], with a stable sediment supply mainly composed of weathered terrigenous clastic material. Due to the relative stability of the sediment source, variations in sediment grain size and composition primarily reflect the influence of climate change rather than changes in the sediment source, providing a reliable foundation for paleoclimate research.

The studied interval consists mainly of interbedded mudstone and sandstone deposited in a shallow-marine shelf setting. Regional sequence-stratigraphic investigations document shelf depositional evolution in the Pearl River Mouth Basin from the late Oligocene to the Miocene [30]. Together with the available lithological logs and biostratigraphic information, these studies provide a framework for evaluating stratigraphic continuity. No major unconformity, large-scale omission, or structural repetition has been identified within the analyzed interval from the available evidence.

The natural GR log from the 3156–3626 m interval of Well L9 was selected for cyclostratigraphic analysis. The interval consists mainly of interbedded mudstone and sandstone and was deposited within a shallow-marine shelf setting. Regional sequence-stratigraphic studies document a persistent shelf depositional framework and systematic depositional evolution in the Pearl River Mouth Basin from the late Oligocene to the Miocene [30]. In addition, the available lithologic and GR logs, biostratigraphic framework, and regional sequence-stratigraphic data do not indicate a regional unconformity, large-scale stratigraphic omission, or structural repetition within the studied interval. The succession is therefore considered suitable for evaluating long-term cyclostratigraphic patterns.

Nevertheless, continuous core coverage and detailed bed-by-bed sedimentological observations are unavailable for the complete studied interval. Localized erosion, sediment reworking, bypass, condensation, and short-duration intraformational hiatuses within individual sandstone-bearing intervals therefore cannot be completely excluded. Such bed-scale processes may locally perturb the GR record and are regarded as a source of uncertainty. However, the orbital components investigated in this study range from approximately 39 kyr to 2.4 Myr and represent stratigraphic variability at tens-of-thousands- to million-year timescales rather than the depositional duration of individual sandstone beds. Accordingly, the astronomical age model developed here is used to characterize long-term depositional rhythms across the studied interval and is not used to determine the actual depositional duration of individual sandstone beds, erosional surfaces, or short-lived condensed intervals.

The GR sampling interval is 0.125 m, which satisfies the Nyquist sampling criterion and provides at least four data points for the estimated thickness of the shortest precession-scale cycle [37].

3.2. Palynological Analysis

The samples were processed following standard palynological preparation procedures [38], without the use of oxidants. First, HCl was used to remove carbonates, followed by HF to remove silicates. The samples were then processed using water washing and sieving techniques. The water washing and sieving were conducted in an ultrasonic cleaner with a sieve mesh size of 10 μm, typically for no more than 2 min. After water washing and sieving, particles larger than 10 μm were collected in a test tube, prepared for slide observation under a transmitted light microscope. To enable quantitative concentration estimates, one *Lycopodium* marker-spore tablet containing 27,637 spores was added to each sample before acid treatment, following the method of Stockmarr [39]. All organic-walled microphytoplankton fossils in the samples were identified and counted using a Leica (DMR) biological microscope. Identification and counting were conducted with at least 100 grains as the basic criterion for achieving a statistically significant palynological assemblage. The analysis of palynological assemblage characteristics was mainly performed using Tilia software, involving statistical analysis, plotting, and cluster analysis of the palynological data to identify and interpret the characteristics of the assemblages [40].

3.3. Foraminiferal Quantitative Analysis

Samples were soaked, heated, and allowed to disaggregate before wet sieving through a 63 μm mesh. The retained fraction was dried and examined under a binocular microscope. Planktonic foraminiferal abundance was recorded semiquantitatively, and the assemblages were assessed using published zonation schemes and regional Oligocene–Miocene records [41–44]. Intervals containing sparse or reworked specimens were treated cautiously when assigning stratigraphic significance.

3.4. Calcareous Nannofossil Analysis

Samples were prepared using the standard smear-slide technique [45]. Smear slides were prepared from small quantities of homogenized sample material following the procedure described by Bown and Young [45]. A water suspension was spread onto a glass slide, dried, and mounted with Eukitt medium. Taxonomic observations were made under polarized light at 1250× magnification. For each sample, specimens were identified and counted across 100 fields of view.

3.5. Establishment of the Biostratigraphic Framework

Prior to cyclostratigraphic analysis and astronomical tuning, an independent biostratigraphic framework was established using calcareous nannofossil and planktonic foraminiferal data. Calcareous nannofossil biozones were identified following the standard zonation schemes of Martini [46] and Okada [47], and the principal bioevents were assigned numerical ages based on GTS2020 [41,42] and published regional biostratigraphic records [48,49]. Planktonic foraminiferal assemblages were evaluated using the zonation scheme of Berggren et al. [43] together with published Oligocene–Miocene biostratigraphic records from the northern South China Sea [44]. The global chronostratigraphic framework follows the current International Chronostratigraphic Chart (v2026/06) of the International Commission on Stratigraphy (ICS) [50].

Because the microfossil samples were collected at discrete depth intervals, the sampled depths of the bioevents were treated as stratigraphic constraints rather than exact boundary positions. The corresponding boundary horizons were interpolated in the continuous GR log using the integrated biostratigraphic and sequence-stratigraphic framework. The resulting age–depth relationship was used to estimate the long-term average sedimentation rate before astronomical tuning. This independently derived estimate was used only to evaluate the geological plausibility of the candidate sedimentation rates identified by the COCO and eCOCO analyses and was not derived from, or adjusted to, the cyclostratigraphic results. The data types, sample numbers, and sampling resolutions are summarized in Table 1.

Table 1. The types, quantities and sampling resolutions of the samples collected and tested in this study.

Data	Sampling Coverage/Resolution	Number
Natural gamma-ray (GR) log	3156–3626 m/0.125 m sampling interval	3757
Palynological samples	3200–3626 m/approximately 5–10 m spacing	44
Calcareous nannofossil samples	3200–3626 m/approximately 5–10 m spacing	48
Foraminiferal samples	3156–3626 m/approximately 10 m spacing	48

3.6. Cyclostratigraphic Analysis and Astronomical Age-Model Construction

Cyclostratigraphic analyses were conducted primarily using Acycle 2.8 [51]. Before spectral analysis, outliers were removed, non-equidistant data were linearly interpolated, and long-term trends were removed using locally weighted scatterplot smoothing (LOWESS). The COCO method was then applied to evaluate the correlation between the power spectrum of the GR record in the depth domain and that of the theoretical astronomical solution under different sedimentation-rate assumptions. The eCOCO method was used to track stratigraphic variations in the optimal sedimentation rate, and 2000 Monte Carlo simulations were performed to test the null hypothesis of no astronomical forcing [52]. The candidate sedimentation-rate solutions were evaluated against the independent age–depth relationship established in Section 3.5.

The multi-taper method (MTM) spectral analysis was subsequently used to identify potential eccentricity, obliquity, and precession components. Evolutionary spectral analysis and wavelet analysis were applied to evaluate the stratigraphic continuity and variation in the detected cyclic signals. Gaussian band-pass filtering was used to extract the approximately 405 kyr long-eccentricity, 100 kyr short-eccentricity, and 41 kyr obliquity components. A floating astronomical age model was first constructed by tuning the identified approximately 405 kyr component to the theoretical long-eccentricity solution [53]. The floating model was then anchored using the independently established biostratigraphic age constraints to construct a biostratigraphically constrained astronomical age model.

To evaluate the proposed long-period orbital modulation, the approximately 40 kyr and 100 kyr components were extracted from the GR record using the filter settings reported in Supplementary Note S4. Their amplitude envelopes were calculated using the Hilbert transform and subsequently examined by spectral analysis. Corresponding components of the astronomical solution of Laskar et al. (2004) [53] were processed using the same procedure to facilitate comparison. The approximately 2.4 Myr and 1.2 Myr filter outputs of the tuned GR series are shown in Figure S2.

4. Results

4.1. Biostratigraphic Framework and Independent Age Constraints

An independent biostratigraphic framework was established before cyclostratigraphic analysis and astronomical tuning, based primarily on calcareous nannofossil bioevents and supplemented by planktonic foraminiferal evidence. Quantitative analysis of 48 calcareous nannofossil samples collected at approximately 10 m intervals between 3155 and 3625 m identified 13 species representing an Oligocene–Miocene assemblage. Details of the principal taxa and biozonal criteria are provided in Supplementary Note S3 and Figure S3.

The last occurrence (LO) of *Reticulofenestra umbilica* was identified at 3535 m and marks the upper boundary of the NP22 Zone in the biozonation adopted here [46]. This bioevent is calibrated at approximately 32.30 Ma [43]. The interval between 3535 and 3205 m was assigned to the combined NP23–NP25 zones [46]. The LO of *Dictyococcites bisectus* [43,48] was identified in the sample at 3205 m and is calibrated at approximately 23.03 Ma, providing the principal biostratigraphic constraint on the Oligocene–Miocene boundary.

Because the calcareous nannofossil samples were collected at discrete depth intervals, the sample at 3205 m constrains but does not precisely locate the Oligocene–Miocene boundary. By integrating this biostratigraphic constraint with the sequence-stratigraphic interpretation of Well L9, the corresponding boundary horizon was placed at 3202 m on the continuous GR log. The 3202 m horizon was therefore used as the continuous-log position of the 23.03 Ma age anchor in the subsequent astronomical tuning.

Planktonic foraminiferal data provide supplementary age constraints. A total of 48 samples from the 3156–3626 m interval were analyzed. The occurrence of the early Oligocene index taxon *Chiloguembelina cubensis* in a sidewall-core sample at 3395 m supports an early Oligocene age for this part of the succession [43,44]. Because foraminifera are scarce in several intervals and reworked specimens occur near the base of the studied section, the foraminiferal record was used mainly to support the stratigraphic assignment and evaluate the calcareous nannofossil biozonation rather than as an independent numerical tuning anchor.

The two principal calcareous nannofossil control levels at 3535 and 3205 m correspond to ages of approximately 32.30 and 23.03 Ma, respectively. The 330 m stratigraphic interval between these control levels represents approximately 9.27 Myr, yielding an approximate pre-tuning long-term average sedimentation rate of 3.56 cm/kyr. This independently derived value provides a geological plausibility check on the candidate sedimentation rates identified by the COCO and eCOCO analyses in Section 4.2.

4.2. Cyclostratigraphic Analysis and Astronomical Age Model

Under the independent biostratigraphic framework established in Section 4.1, cyclostratigraphic analysis was performed on the natural gamma-ray record from the 3156–3626 m interval of Well L9. The COCO and eCOCO methods were applied to the detrended GR series to evaluate the correlation between the observed sedimentary spectrum and theoretical astronomical periods under different sedimentation-rate assumptions (Figure 2) [52]. The independently established biostratigraphic age–depth relationship was used as a geological criterion for evaluating the plausibility of the candidate sedimentation-rate solutions.

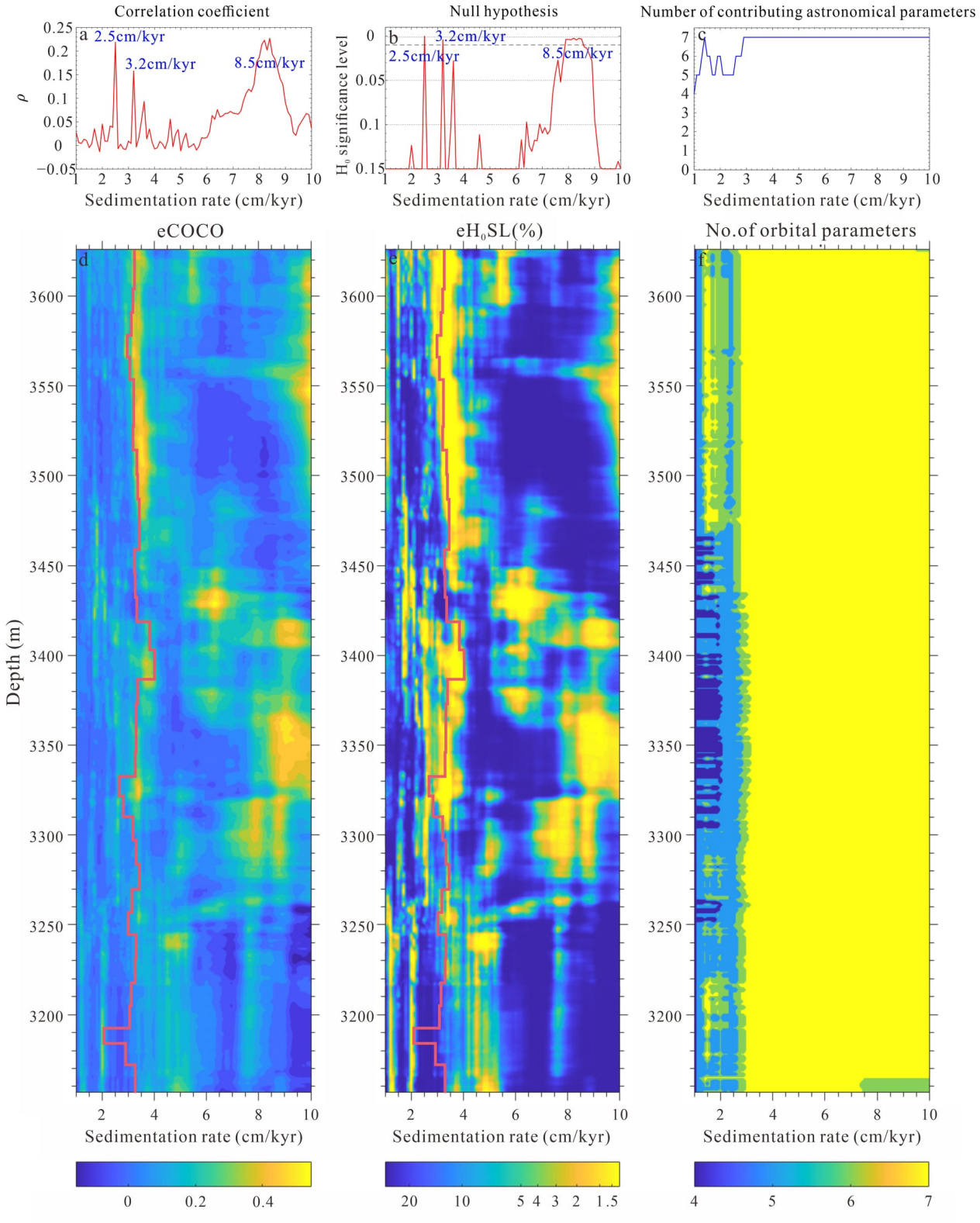


Figure 2. The COCO and eCOCO analysis results for the GR data sequence from Well L9 (3156–3626 m) involved testing sedimentation rates in the range of 1–10 cm/kyr, with a step increment of 0.1 cm/kyr, and conducting 2000 Monte Carlo simulations. (**a**–**c**) Correlation coefficients, null hypothesis significance level, and number of contributing astronomical parameters involved. (**d**–**f**) Evolutionary correlation coefficient, evolutionary H0 significance level, and number of contributing astronomical parameters. The red line represents the sedimentation rate.

Sedimentation rates ranging from 1 to 10 cm/kyr were tested using 2000 Monte Carlo simulations. Significant COCO solutions were identified at approximately 2.5, 3.2, and 7.9–8.5 cm/kyr, all with null-hypothesis significance levels below 0.1%. Statistical significance alone, however, does not establish the geological plausibility of a candidate solution.

The independently dated interval between 3535 and 3205 m is 330 m thick and spans approximately 9.27 Myr, corresponding to a long-term average sedimentation rate of approximately 3.56 cm/kyr. A sedimentation rate of 2.5 cm/kyr would imply a duration of approximately 13.2 Myr for this interval, whereas rates of 7.9–8.5 cm/kyr would imply durations of only approximately 3.9–4.2 Myr. Both estimates differ markedly from the independently constrained biostratigraphic duration. In addition, the approximately 2.5 cm/kyr solution is supported by only five contributing astronomical parameters, whereas the 7.9–8.5 cm/kyr solution is not persistently reproduced by the eCOCO analysis.

In contrast, the COCO maximum at approximately 3.2 cm/kyr is close to the independently estimated value of approximately 3.56 cm/kyr, and the eCOCO-derived range of approximately 2.9–4.1 cm/kyr encompasses this independent estimate. A comparable regional sedimentation rate was reported at IODP Site U1501 in the northern South China Sea, where the upper late Oligocene to lower early Miocene interval accumulated at approximately 35 mm/kyr (3.5 cm/kyr) [54]. This value is close to the independently estimated rate for Well L9 and provides additional regional support for the geological plausibility of the preferred sedimentation-rate range. Because Site U1501 represents a different depositional setting, this comparison is used only as supporting regional evidence rather than as an independent chronological constraint. The range of approximately 2.9–4.1 cm/kyr is therefore regarded as the preferred and geologically most plausible sedimentation-rate solution for the studied interval.

MTM spectral analysis and evolutionary spectral analysis of the GR record in the depth domain identified significant sedimentary cycles of approximately 84.8, 44.8, 15.1, 3.5, and 1.5 m (Figure 3). Under the sedimentation-rate range constrained above, these cycles are interpreted as the sedimentary expressions of the approximately 2.4 Myr long eccentricity modulation, 1.2 Myr obliquity modulation, 405 kyr long eccentricity, approximately 100 kyr short eccentricity, and approximately 39 kyr obliquity cycles, respectively. The approximately 470 m succession represents an estimated duration of approximately 12.86 Myr, with a mean sedimentation rate of approximately 3.6 cm/kyr.

The approximately 15.1 m component was tuned to the theoretical 405 kyr long-eccentricity solution [53]. Based on the independent biostratigraphic framework established in Section 4.1, the calibrated ages of the relevant bioevents from GTS2020 and regional biostratigraphic records [41–44,48], and the current ICS chronostratigraphic framework [50], an age of approximately 23.03 Myr was assigned to the Oligocene–Miocene boundary. The boundary was constrained by the calcareous nannofossil sample at 3205 m and correlated to the 3202 m horizon on the continuous GR log. The 3202 m horizon was subsequently used as the principal age anchor for astronomical tuning. This procedure produced a biostratigraphically constrained astronomical age model spanning approximately 34.6–21.7 Myr.

Spectral analysis of the tuned GR record identified significant peaks at approximately 2.4 Myr, 1.2 Myr, 405 kyr, 95 kyr, 52 kyr, and 39 kyr (Figure 3), broadly corresponding to the theoretical astronomical solution. The consistent spectral patterns in the depth- and time-domain records indicate that the astronomical tuning preserves the principal cyclic characteristics of the original GR series.

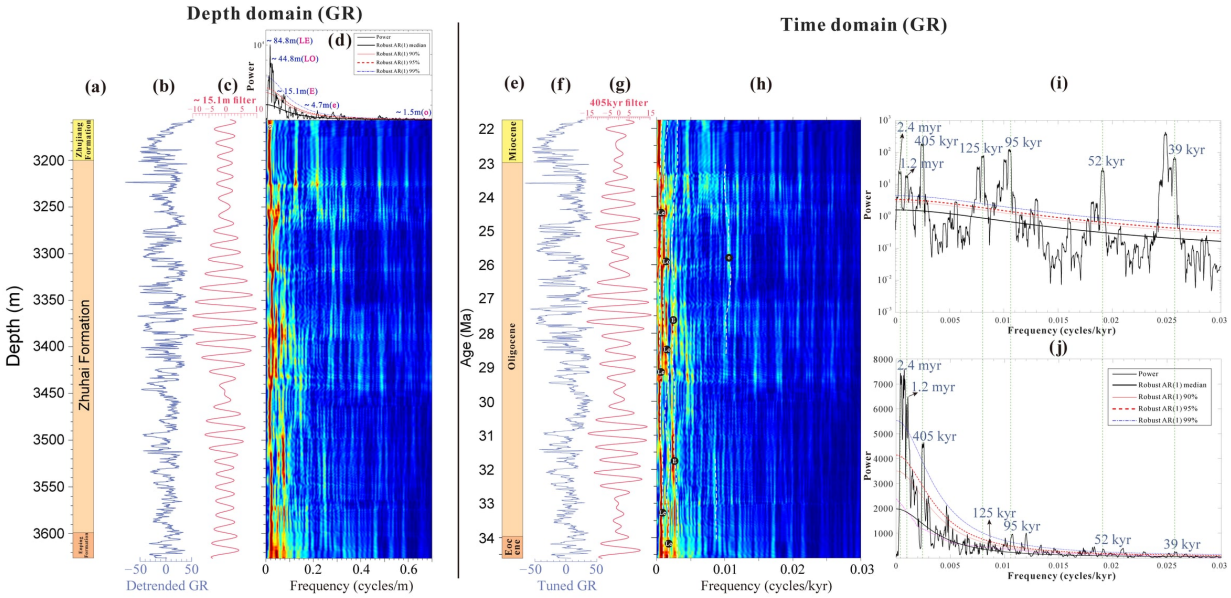


Figure 3. The cyclostratigraphic analyses of the GR series of Well L9. (**a**) Change in lithology of Well L9. (**b**) Well L9 35% weighted average detrended GR series from 3156 m to 3626 m (blue solid curve). (**c**) A ~15.1 m filter output of the detrended GR data in the depth domain (passband: 0.066 ± 0.006 cycles/m, red solid curve from the Gauss filter). (**d**) 2π MTM power spectrum of the detrended GR series is also shown with a background robust AR (1) model, and at 90%, 95%, and 99% significance levels. (**e**) Evolutionary spectrogram of the detrended GR data in the depth domain (evolutionary power spectrum calculated using a 100 m sliding window with a 0.819 m step). (**f**) The tuned GR time series. (**g**) Approximately 405 kyr eccentricity cycles filter output of the tuned GR data in the time domain (passband: 0.0247 ± 0.005 cycles/kyr, red solid curve from the Gauss filter). (**h**) Evolutionary spectrogram of the tuned GR data in the time domain (evolutionary power spectrum calculated using a 3000 kyr sliding window with a 20 kyr step). (**i**) ETP astronomical solution for 22 to 34.5 Myr [53]. (**j**) 2π MTM power spectrum of the detrended, tuned GR time series. Red dashed lines on power spectra are the 95% significance levels. And significant Milankovitch peaks are labelled with blue numbers. Labels on the power spectrum are 2.4 Myr extra-long eccentricity (LE), 1.2 Myr extra-long obliquity (LO), 405 kyr long eccentricity (E), 125 kyr short eccentricity (e), and 41 kyr obliquity (o).

4.3. Amplitude Modulation of the Short-Period Orbital Components

To evaluate the orbital origins of the long-period cycles observed in the GR record, amplitude-envelope analyses were performed on the extracted short-period components (~40 kyr and ~100 kyr) and compared with the theoretical astronomical solutions (La04) [53]. The results reveal distinctly different long-period amplitude modulation structures (Figure 4).

For the obliquity band, spectral analysis of the ~40 kyr GR amplitude envelope identifies a prominent component near 1.2 Myr, which is supported by F-test significance levels exceeding the 95% confidence threshold (Figure 4a). This observed ~1.2 Myr modulation is highly consistent with the theoretical amplitude modulation of obliquity in the La04 astronomical model (Figure 4b), strongly supporting an obliquity-related origin for this sedimentary signal.

In contrast, the amplitude modulation of the short-eccentricity band presents a notable discrepancy. Spectral analysis of the ~100 kyr GR amplitude envelope exhibits a statistically significant peak (F-test > 95%) centered at approximately 1.6 Myr (Figure 4c). Notably, it lacks a clear, statistically significant peak at the 2.4 Myr period, which is the dominant long-eccentricity modulation period expected from the La04 theoretical model (Figure 4d). Consequently, the carrier-band analyses do not fully reproduce the expected ~2.4 Myr

eccentricity modulation, indicating that the ~1.6 Myr variability observed in the 100 kyr envelope requires further interpretation regarding its origin.

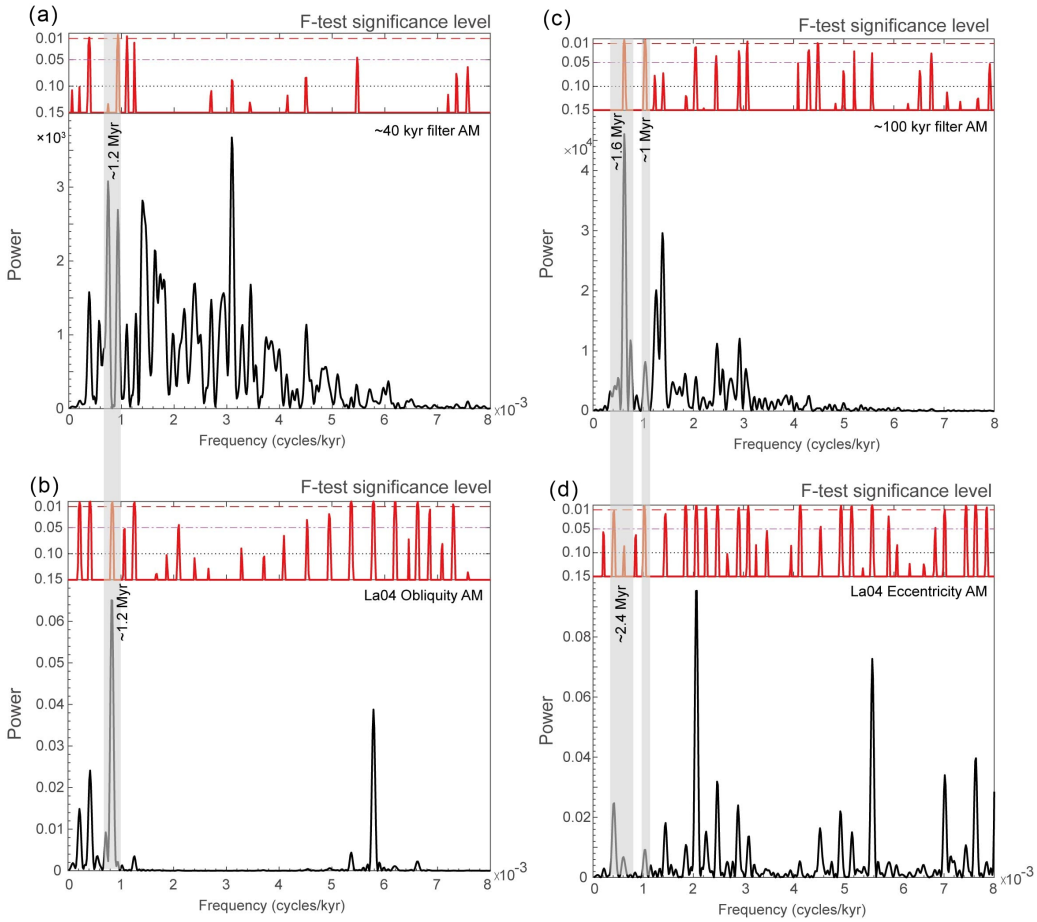


Figure 4. Spectral analyses of the amplitude modulations (AMs) of the short-period orbital components extracted from the tuned GR data in Well L9 (spanning ~34.6 to 21.8 Ma) compared with the theoretical astronomical solutions (La04) [53]. (**a**) Periodograms (black line) and F-test significance levels (red line) of the amplitude envelope of the ~40 kyr obliquity component from the tuned GR data. A statistically significant peak is observed near 1.2 Myr. (**b**) Periodograms of the amplitude modulation of theoretical obliquity from the La04 astronomical model, highlighting the expected ~1.2 Myr cycle. (**c**) Periodograms (black line) and F-test values (red line) of the amplitude envelope of the ~100 kyr short-eccentricity component from the tuned GR data, showing a dominant peak near 1.6 Myr. (**d**) Periodograms of the amplitude modulation of theoretical eccentricity from the La04 model, displaying the expected strong 2.4 Myr long-eccentricity cycle. Horizontal dashed lines indicate the 90%, 95%, and 99% confidence levels for the F-test.

4.4. Palynological Assemblage Characteristics

A total of 44 pollen samples were analyzed and identified from Well L9, with an average sampling interval of approximately 5–10 m, covering the depth range from 3200 to 3626 m. Pollen content in the assemblages showed significant dominance, ranging from 61.4% to 99.0%. A total of 67 pollen species were identified, including 11 species of fern spores, 7 species of gymnosperm pollen, and 49 species of angiosperm pollen. Planktonic algae were also observed, with content ranging from 1.0% to 38.6%. Twenty species of planktonic algae were identified, including 4 species of lacustrine and fluvial algae and 16 species of marine dinoflagellates (Figure 5). In terms of pollen types, the fern spores (*Polypodiaceaesporites* spp., (Potonié, 1951), *Polypodiisporites* spp., (Potonié, 1956), *Toroisporis* sp., (Krutzsch, 1959), *Cyathidites* sp., (Couper, 1953), *Deltoidospora* spp., (Miner,

1935), *Extrapunctatosporites* spp., (Krutzsch, 1959), *Osmundacidites wellmanii*., (Couper, 1953)) are all tropical–subtropical, hygrophilous pollen. Gymnosperm pollen is dominated by pine, which occurs in tropical to temperate climates. The dominant angiosperms, *Q. minutus* and *Q. microhenrici* (Thiergart, 1950), occupy a similar climatic range and indicate humid conditions. Overall, forest vegetation and subtropical–temperate climatic elements predominate (Figure 6). Marine dinoflagellates tolerant of brackish-water influence are dominant in several intervals, suggesting variable freshwater influence within a shallow-marine shelf setting [17,55]. The main pollen content, assemblage names, and geological ages of Well L9 are detailed in the pollen statistics for Well L9 (Supplementary Note S2). The numerical ages assigned to the palynological record are based on the biostratigraphically constrained astronomical age model established in Section 4.2.

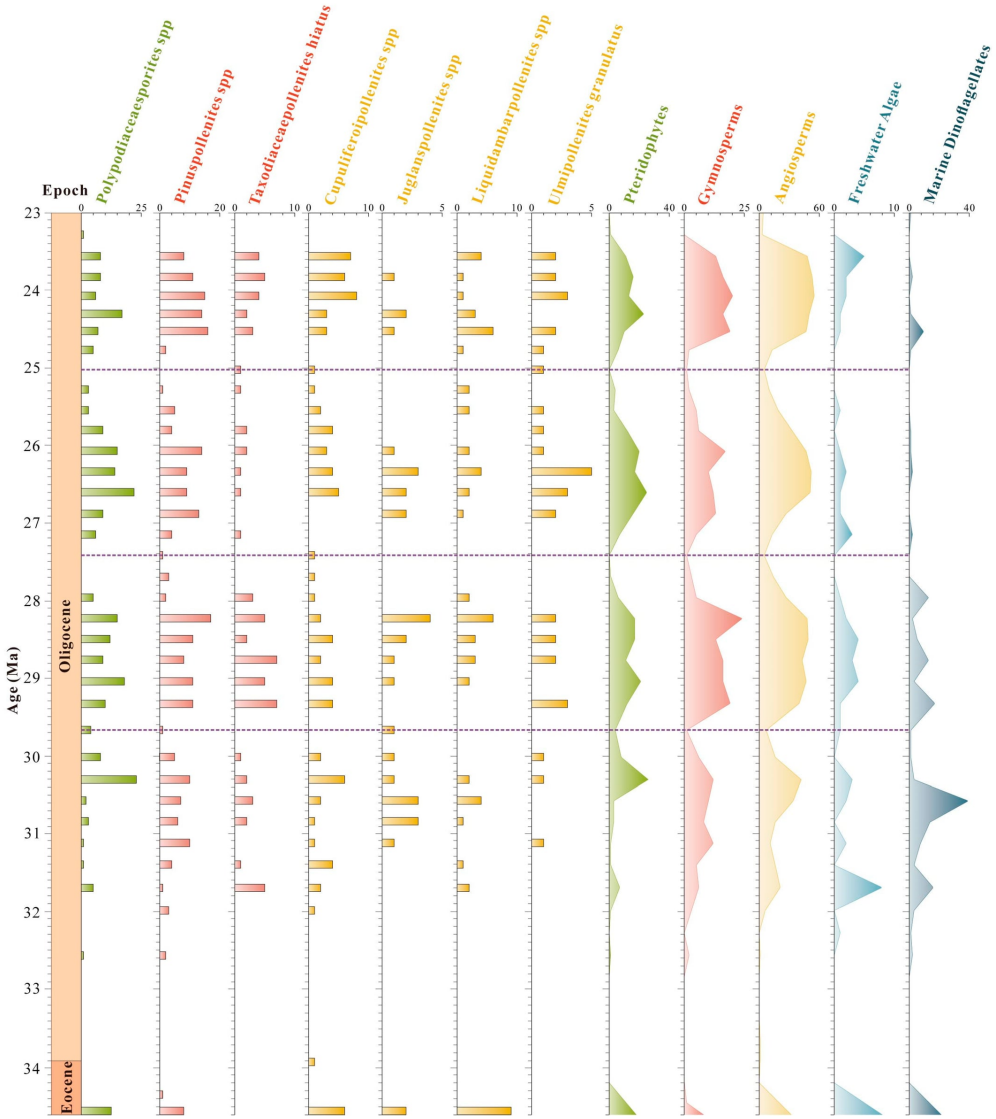


Figure 5. Vertical variation in the main pollen and algal records from the Oligocene in the Pearl River Mouth Basin, South China Sea. Figure shows pteridophytes in green, gymnosperms in red, angiosperms in yellow, freshwater algae in blue, and marine dinoflagellates in dark blue.

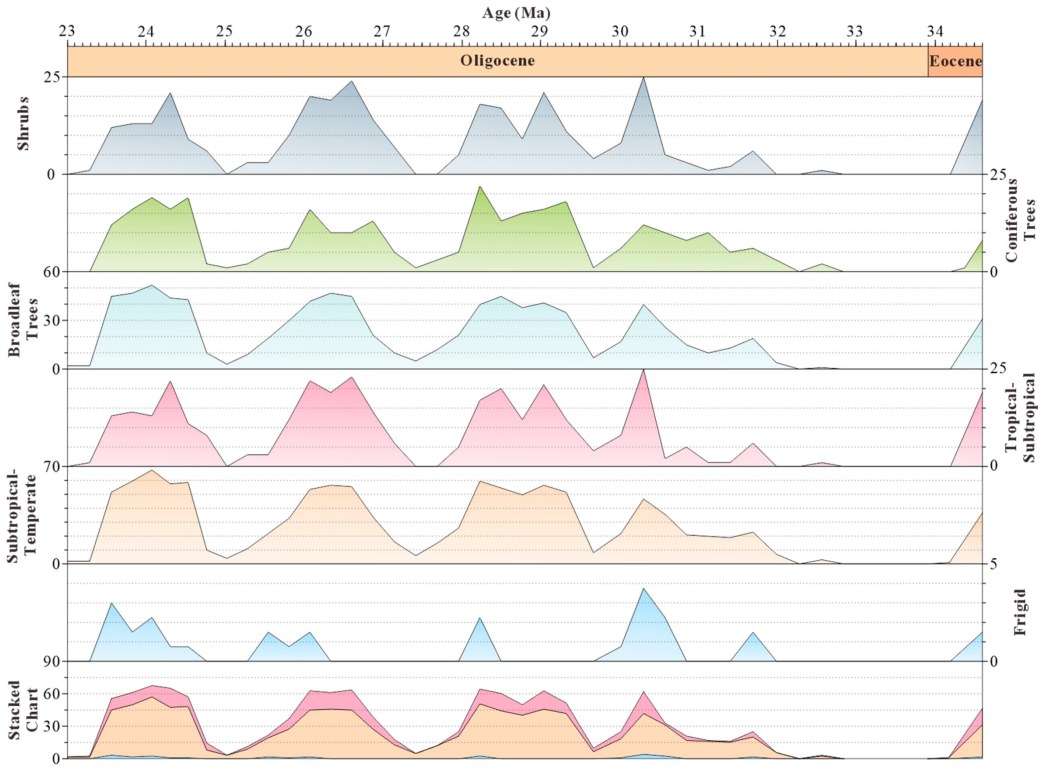


Figure 6. Comparison of vegetation and climate zone dynamics during the Eocene–Oligocene in the Pearl River Estuary Basin, South China Sea. The last chart is a climatic zone stacked chart.

4.5. Calcareous Nannofossil Assemblages and Paleoenvironmental Changes

Quantitative analysis of the 48 calcareous nannofossil samples identified marked stratigraphic changes in abundance, diversity, and assemblage composition. The biochronological significance of the diagnostic taxa and the corresponding biozonation are presented in Section 4.1. Based on the biostratigraphically constrained astronomical age model established in Section 4.2, the paleoenvironmental changes recorded by the calcareous nannofossil assemblages can be divided into three stages (Figure 7).

During the first stage, from approximately 34.6 to 29.1 Ma, calcareous nannofossils were generally abundant, reaching a maximum of 1140 specimens per 100 fields of view. Although several samples contained fewer specimens, most yielded more than 100 specimens per 100 fields of view. Species richness ranged from 1 to 13 and was commonly greater than 5. The relatively high abundance of *Discoaster* suggests a stronger open-marine influence. Together with the lithological and other microfossil evidence, the assemblage indicates a shallow-marine shelf setting with appreciable open-marine influence.

During the second stage, from approximately 29.1 to 23.9 Ma, calcareous nannofossils were scarce and occurred only sporadically in a limited number of samples. The reduction in abundance and diversity is consistent with relative shallowing toward a more proximal shelf setting and with less favorable conditions for calcareous nannoplankton productivity or preservation.

During the third stage, from approximately 23.9 to 21.7 Ma, nannofossil diversity was generally lower than 10. *Discoaster* remained relatively abundant, whereas *Umbilicosphaera* was less common. The assemblage indicates renewed open-marine influence within the shallow-marine shelf setting.

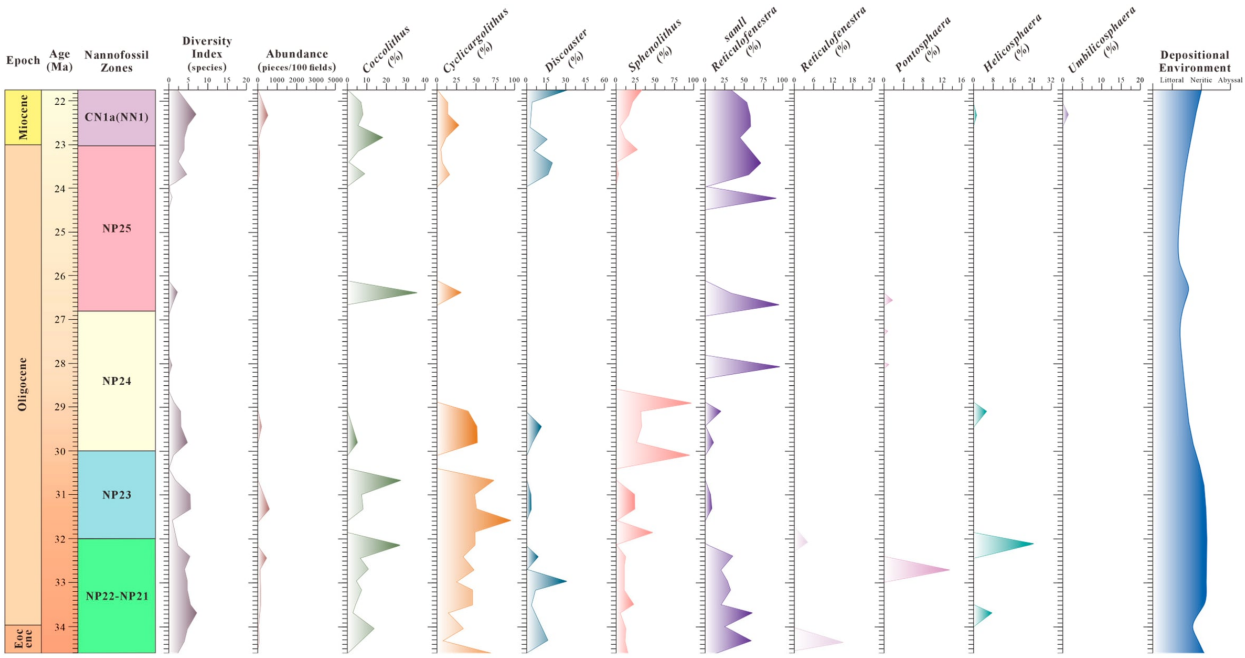


Figure 7. Relative abundances (%) of the main components of the calcareous nannofossil assemblages and depositional environment from Well L9.

4.6. Foraminiferal Assemblages and Paleoenvironmental Changes

A total of 48 foraminiferal samples from the 3156–3626 m interval of Well L9 were analyzed. Foraminifera are extremely scarce between 3265 and 3435 m, and several samples are nearly barren. Reworked specimens occur near the base of the studied succession, whereas moderate to abundant planktonic foraminifera occur in parts of the middle and upper intervals. The biostratigraphic implications of the foraminiferal record are presented in Section 4.1.

Planktonic foraminifera first become consistently represented near 3625 m and increase upward, with relatively high abundances between approximately 3595 and 3535 m. This change indicates relative deepening within the shelf system, from a shallower shelf setting to a more distal shelf setting, at approximately 34 Ma. Between approximately 3525 and 3435 m, planktonic foraminifera decrease markedly and subsequently become nearly absent in several samples, indicating a shift toward a shallower and more proximal shelf setting between approximately 29 and 26 Ma.

A pronounced increase in planktonic foraminiferal abundance near 3205 m, together with evidence of enhanced calcification, indicates marine deepening and a relative highstand after approximately 23 Ma. From the latest Oligocene into the Miocene, the foraminiferal assemblages indicate a relatively stable and more distal shelf environment. The relatively thin Miocene succession and the high proportion of fragmented tests may additionally reflect deposition in a more distal shelf setting than during much of the Oligocene (Figure 8).

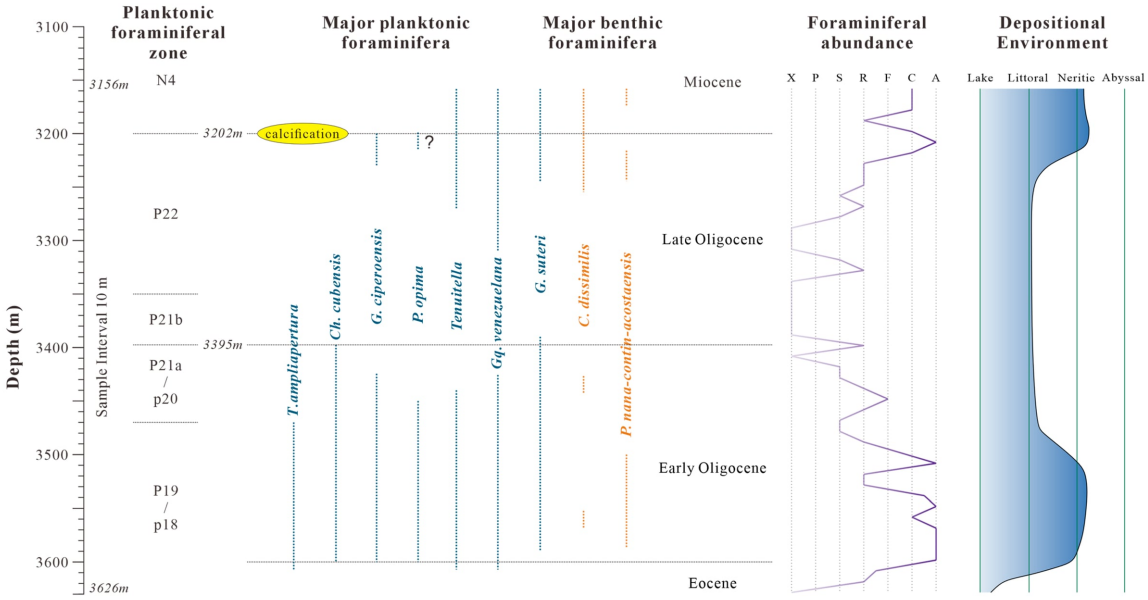


Figure 8. The distribution and abundance variation in foraminifera in Well L9, along with the sedimentary environment, are represented in the chart. The blue dashed line indicates the main planktonic foraminifera, while the orange dashed line represents the main benthic foraminifera. In the context of foraminiferal abundance, the following classifications are used: A = abundant, C = common, F = frequent, R = rare, S = sporadic, P = present, and X = none (planktonic foraminiferal zone [18]).

5. Discussion

5.1. Multi-Proxy Constraints on Paleoclimate Reconstruction

The paleoclimate reconstruction for Well L9 is based on the integrated interpretation of natural gamma-ray (GR), palynological, calcareous nannofossil, and foraminiferal records. Rather than interpreting these proxies independently, each dataset is used to constrain a different component of the climate–sediment system. Palynological assemblages provide the principal evidence for terrestrial vegetation and regional temperature and moisture conditions [56–60]. Under conditions of relatively stable sediment provenance, variations in GR mainly reflect changes in fine-grained terrigenous input and regional hydrological conditions [34,35]. Calcareous nannofossils and foraminifera primarily constrain biostratigraphy and marine depositional environments, while also providing supplementary paleoenvironmental information [43,44,46,61–67].

Microfossil abundance and preservation may additionally be influenced by water depth, dissolution, reworking, and diagenesis [68]. Therefore, interpretations of paleoclimate and depositional water depth in this study are based on the combined evidence from palynological assemblages, marine microfossils, lithology, and well-log data, rather than on any single proxy [69]. This multi-proxy framework provides the basis for the reconstruction of Oligocene paleoclimate evolution presented in Section 5.3.

5.2. Sedimentary Expression and Possible Orbital Origins of Cyclic Variability in the South China Sea

The GR record from Well L9 contains approximately 405 kyr, 100 kyr, and 40 kyr components, together with longer-period variability near 2.4 Myr and 1.2 Myr. Within the 405 kyr cycle-counted, stratigraphically anchored chronology, these features are consistent with a potential orbital contribution to sedimentary variability. However, similarity between observed and astronomical periods does not by itself establish an orbital origin, particularly for the longest components, which are represented by relatively few cycles.

The amplitude-envelope analyses provide different levels of support for the proposed long-period assignments. Approximately 1.2 Myr variability in the 40 kyr envelope is comparable to the obliquity modulation identified in the astronomical reference and supports an obliquity-related interpretation. This agreement concerns modulation period rather than an independently established absolute phase relationship. In contrast, the ~100 kyr envelope exhibits a dominant periodicity near 1.6 Myr rather than the theoretically expected 2.4 Myr component (Figure 4c,d). Although a ~2.4 Myr variability is observed directly in the untuned GR series, its absence in the short-eccentricity amplitude modulation suggests that the orbital signal was significantly altered during its transfer into the sedimentary record. The emergence of this ~1.6 Myr cycle, rather than the expected 2.4 Myr signal, can be attributed to several potential mechanisms. First, nonlinear climatic and sedimentary responses within the shallow-marine shelf setting, such as threshold effects related to sea-level fluctuations, could distort the original orbital forcing, leading to signal truncation and the generation of combination tones or harmonics in the spectral domain. Second, the Pearl River Mouth Basin experienced complex tectonic evolution and active deltaic progradation during the Oligocene [28–30,70]. Episodic tectonic subsidence pulses or autocyclic deltaic lobe switching on million-year timescales might have generated strong regional sedimentary rhythms (~1.5–2.0 Myr) that interfered with or masked the astronomically driven eccentricity envelope. Finally, despite the construction of a robust 405-kyr tuned age model, potential sub-orbital sedimentation rate variations or localized minor sedimentary hiatuses (as noted in Section 3.1) could compress or stretch the true 2.4 Myr signal in the time domain, resulting in a ~1.6 Myr spectral artifact. Consequently, while an orbital origin cannot be entirely ruled out, the current envelope results highlight the complex interplay between astronomical forcing and local depositional dynamics, making the direct attribution of the long-period signal solely to eccentricity modulation uncertain.

Several processes could transmit orbital variability into a low-latitude marginal-sea succession. Eccentricity modulates precessional amplitude [53,71] and may thereby influence seasonal insolation [72], precipitation, catchment weathering, and terrigenous sediment delivery [73–75]. Obliquity-related changes in high-latitude insolation may influence ice-sheet dynamics [76,77] and meridional heat transport, potentially affecting lower-latitude climate [78–81]. Changes in ice volume [77,82] and ocean circulation [83] could also modify marine depositional conditions [84,85]. These pathways provide a conceptual context for interpreting the cyclic record, but their relative contributions cannot be distinguished from periodicity alone.

In Well L9, GR variations may reflect a combination of hydrological changes, sediment delivery, grain-size sorting, and shifts in depositional conditions. The available evidence does not independently establish an ice-volume or sea-level origin for the observed long-period variability. We therefore regard orbital–hydrological and high-latitude climatic influences as plausible pathways rather than demonstrated mechanisms.

5.3. Oligocene Paleoclimate Evolution Recorded in the South China Sea

The Pearl River Mouth Basin in the South China Sea, owing to its unique geographical location, offers valuable records for studying climate evolution during the Oligocene [17,55]. Pollen assemblage analysis results show that arboreal plants (including conifers and broadleaf trees) dominate, consistent with a humid environment [56], while xerophytic plants are relatively scarce. Specifically, the proportion of tropical–subtropical pollen plants in each stratigraphic section is less than 30%, the proportion of subtropical–temperate pollen plants exceeds 60%, and the proportion of xerophytic pollen plants is less than 20%. According to the classification standard by Zhong et al. [86], a proportion of subtropical–temperate pollen plants exceeding 30% indicates that the region belongs to the subtropical–temperate

climatic zone, while a proportion of xerophytic pollen plants below 20% suggests a humid climate. Both qualitative and quantitative analyses of the pollen assemblages indicate that the overall climate during this period was cool, humid, and in the subtropical–temperate zone (Figure 5). The stratigraphic framework of the Oligocene succession in the Pearl River Mouth Basin is constrained by standard biostratigraphic zonation schemes [43,44,46,47] and correlated with the current ICS International Chronostratigraphic Chart (v2026/06) [50]. Calcareous nannofossil and planktonic foraminifera biohorizons identified in our core samples define discrete Rupelian and Chattian intervals, offering independent biostratigraphic age constraints to anchor our astronomical tuning results and stratigraphic climate records. This biostratigraphic division provides a fundamental chronological basis for distinguishing cooling events across the early to late Oligocene.

The calcareous nannofossil assemblages reveal changes in relative abundance during the Oligocene (Figure 7), demonstrating the link between paleoclimate changes and the response of local phytoplankton communities [61]. Particularly, the calcareous nannofossil small *Reticulofenestra* is highly sensitive to climate change [87,88], and it developed throughout the Oligocene, showing a clear response to several significant cooling events. This may represent an adaptive strategy in response to climate change and environmental stress. The records of these microfossils provide important evidence of climate change during the Oligocene.

In contrast, foraminiferal abundance showed an increasing trend during colder periods, which is attributed to the dominance of *Tenuitella* in the foraminiferal samples in this study. *Tenuitella* is a cold-adapted foraminifer that can survive and reproduce in cold environments, indicating its preference for cold waters, a characteristic that has been confirmed in several studies. This also explains why foraminiferal abundance shows a declining trend during the Rupelian stage.

The paleoclimate interpretation inferred from microfossils is further supported by the $CaCO_3$ content at ODP Site 1218 [6]. Lower $CaCO_3$ content typically indicates glacial periods or cold, arid climatic conditions, during which higher concentrations of carbon dioxide in the oceans and lower water temperatures lead to increased dissolution of $CaCO_3$. Simultaneously, lower rates of terrestrial weathering result in reduced calcium ion transport by rivers, and lower marine productivity, thereby limiting both the formation and preservation of calcium carbonate [89,90].

These indicators collectively suggest that the Oligocene climate was generally cool and humid, maintaining relatively low temperatures, with a warming trend emerging during the late Oligocene (Figure 9). The Rupelian stage was colder than the Chattian stage, indicating that the Oligocene underwent a relatively cold period that gradually warmed during the later stages. Additionally, the comparison of GR value variations in this study with global carbon and oxygen isotope records further supports this conclusion [91]. The GR values in the study area, along with carbon isotope ($\delta^{13}C$) and oxygen isotope ($\delta^{18}O$) data, indicate that during the Rupelian stage, higher GR and $\delta^{18}O$ values reflected colder temperatures and larger ice sheets, while lower $\delta^{13}C$ values suggested lower biological productivity and carbon storage. In contrast, during the Chattian stage, the decrease in GR and $\delta^{18}O$ values reflected the retreat of ice sheets and rising temperatures, while changes in $\delta^{13}C$ values indicated variations in biological productivity.

Additionally, the Eocene–Oligocene Transition (EOT) cooling event around 34.3 Ma caused a rapid rise in global oxygen isotopes and a sharp decrease in GR values in the study area, along with a significant reduction in the abundance of the small calcareous nannofossil *Reticulofenestra*, a decrease in pollen quantity, and an increase in the abundance of the cold-adapted planktonic foraminifer *Tenuitella*. These changes reflect the strong and rapid response of microfossils to climate change [56,61,88]. During the climate evolution of

the Oligocene, the corresponding changes in natural gamma data, microfossils, carbon and oxygen isotopes, and $CaCO_3$ exhibit similar response characteristics to cooling events [6,91]. The significant changes in fossil content and abundance clearly reflect the dramatic shifts in microfossil communities triggered by cooling events.

After comparison with published climate records (Figure 9), we identified six major cooling events during the Oligocene: the Oi-1 cooling event around 33.9 Ma, the Oi-1a cooling event around 31.3 Ma, the Oi-2 cooling event around 29.8 Ma, the Oi-2a cooling event around 27.8 Ma, the Oi-2b cooling event around 26.2 Ma [6,91], and the Mi-1 cooling event around 23 Ma [92,93]. The identification of these events provides strong evidence for further research into climate change and extreme climate events during the Oligocene.

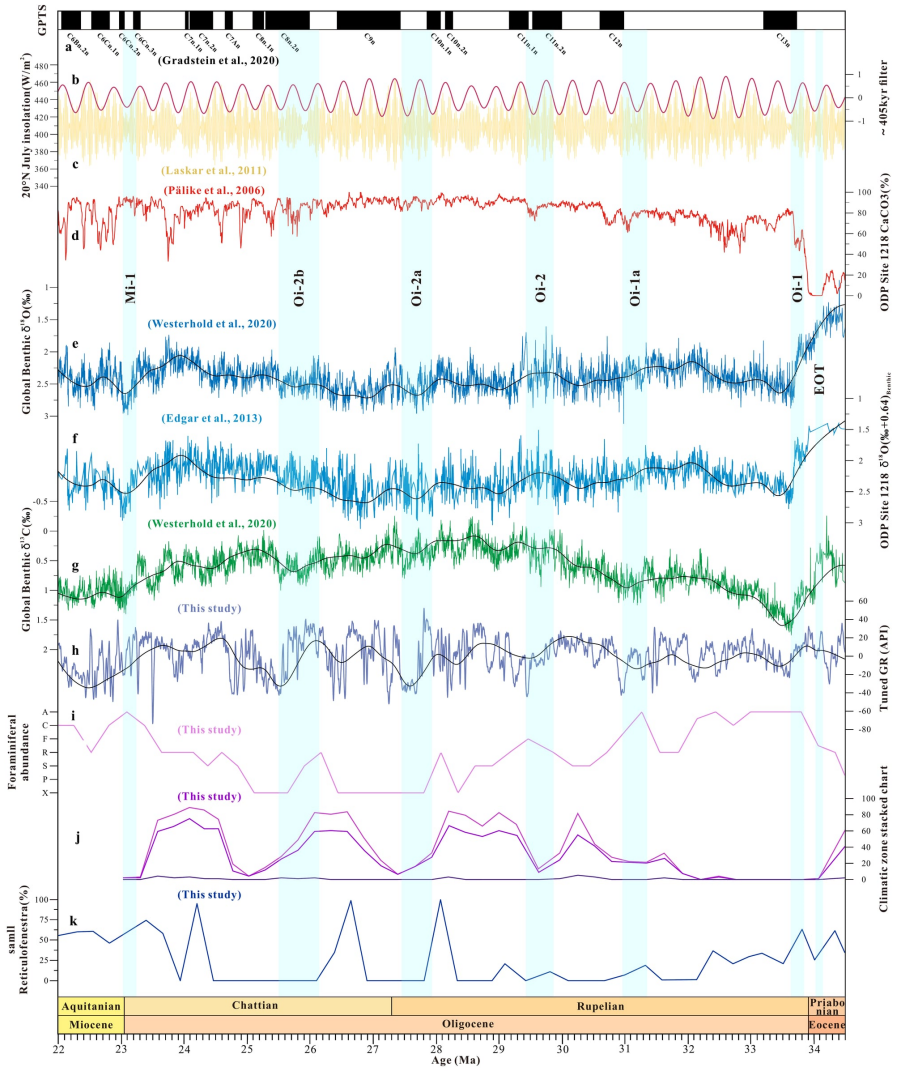


Figure 9. Paleoclimatic changes during the Oligocene. (**a**) Oligocene geomagnetic polarity time scale (GPTS 2020) [94]. (**b**,**c**) The summer mean insolation at 20° N and 405 ka eccentricity variability [53]. (**d**) Calcium carbonate content, ODP Site 1218 [6]. (**e**) Global benthic foraminiferal oxygen isotopes ($\delta^{18}O$) [91]. (**f**) ODP Site 1218 benthic foraminiferal oxygen isotopes ($\delta^{18}O$) [68]. (**g**) Global benthic foraminiferal carbon isotopes ($\delta^{13}C$) [91]. (**h**) Tuned GR series data for Well L9. (**i**) Changes in the abundance of foraminifera in the L9 well (A = abundant, C = common, F = frequent, R = rare, S = sporadic, P = present, X = none). (**j**) Vegetation delineation climatic zone stacked chart for Well L9, tropical–subtropical, subtropical–temperate, and frigid, respectively, from top to bottom. (**k**) The changes in the abundance of small *Reticulofenestra* in the L9 well's calcareous nannofossils. The black smoothed curve is fitted using the locally estimated scatterplot smoothing (LOESS) method with MATLAB R2022a. The vertical blue shading indicates the approximate timing of cooling events.

6. Conclusions

This study establishes a high-resolution, stratigraphically constrained astronomical framework for the Oligocene (approximately 34.6 to 21.7 Ma) in the northern South China Sea. By integrating natural gamma-ray logs with terrestrial and marine microfossil records, we demonstrate that sedimentary variability in this shallow-marine shelf setting was strongly paced by orbital forcing. Our findings highlight the complex nature of orbital signal preservation in marginal sea environments. While long-period obliquity modulation is robustly recorded, the distortion of the expected long-eccentricity envelope suggests that global astronomical signals can be significantly overprinted by non-linear depositional responses, threshold effects, or regional tectonic dynamics. This underscores the necessity of critically evaluating the origins of long-period sedimentary cycles rather than assuming direct orbital forcing based solely on spectral periodicity.

Furthermore, the multi-proxy paleoclimate reconstruction reveals a distinct climatic evolution, transitioning from generally cool and humid conditions in the early–middle Oligocene to a warming trend in the late Oligocene. The observed shifts in palynological assemblages and marine microfossils broadly correspond to recognized global Oligocene cooling episodes, confirming the sensitivity of the South China Sea margin to global climate fluctuations.

Ultimately, this research provides a vital regional paleoenvironmental framework. To further disentangle the complex linkages between astronomical forcing, global climate events, and local depositional dynamics, future work should prioritize continuous sedimentological coring and multi-site correlations across the basin.

Supplementary Materials: The following supporting information can be downloaded at: https://www.mdpi.com/article/10.3390/geosciences16110474/s1, Supplementary Note S1: Optimal Data Sequence Selection; Supplementary Note S2: Palynological Analysis; Supplementary Note S3: Calcareous Nannofossil Analysis; Supplementary Note S4: Analytical workflow and parameter settings; Figure S1: Structural configuration of the Baiyun Depression and location of Well L9; Figure S2: Time domain filtering curves of tuned GR series from Well L9; Figure S3: Distribution and stratigraphic delineation of calcareous nannofossils in Well L9.

Author Contributions: Conceptualization, Y.Z. and X.L.; methodology, Y.Z., E.X. and S.Z.; software, Y.Z. and E.X.; validation, Y.Z. and E.X.; formal analysis, Y.Z., Y.W. and E.X.; investigation, Y.Z., S.Z.; resources, X.L.; data curation, Y.Z. and E.X.; writing—original draft preparation, Y.Z. and E.X.; writing—review and editing, X.L., S.Z.; visualization X.L., Y.Z. and E.X.; supervision, X.L. and S.Z.; project administration, X.L. and Y.W.; funding acquisition, X.L. All authors have read and agreed to the published version of the manuscript.

Funding: The work was supported by the National Natural Science Foundation of China (grant No. 41472098).

Data Availability Statement: All data and materials are available on request from the corresponding author. The data are not publicly available due to ongoing research using part of the data.

Conflicts of Interest: Author Enze Xu is employed by the company China Southern Petroleum Exploration & Development Corporation. The remaining authors declare that the research was conducted in the absence of any commercial or financial relationships that could be construed as a potential conflict of interest.

References

1. De Lira Mota, M.A.; Dunkley Jones, T.; Sulaiman, N.; Edgar, K.M.; Yamaguchi, T.; Leng, M.J.; Adloff, M.; Greene, S.E.; Norris, R.; Warren, B.; et al. Multi-Proxy Evidence for Sea Level Fall at the Onset of the Eocene-Oligocene Transition. *Nat. Commun.* **2023**, *14*, 4748. [CrossRef] [PubMed]
2. Hochmuth, K.; Whittaker, J.M.; Sauermilch, I.; Klocker, A.; Gohl, K.; LaCasce, J.H. Southern Ocean Biogenic Blooms Freezing-in Oligocene Colder Climates. *Nat. Commun.* **2022**, *13*, 6785. [CrossRef] [PubMed]

3. Moore, T.C., Jr.; Wade, B.S.; Westerhold, T.; Erhardt, A.M.; Coxall, H.K.; Baldauf, J.; Wagner, M. Equatorial Pacific Productivity Changes near the Eocene-Oligocene Boundary. *Paleoceanography* **2014**, *29*, 825–844. [CrossRef]
4. Zachos, J.; Pagani, M.; Sloan, L.; Thomas, E.; Billups, K. Trends, Rhythms, and Aberrations in Global Climate 65 Ma to Present. *Science* **2001**, *292*, 686–693. [CrossRef] [PubMed]
5. Ao, H.; Liebrand, D.; Dekkers, M.J.; Zhang, P.; Song, Y.; Liu, Q.; Jonell, T.N.; Sun, Q.; Li, X.; Li, X.; et al. Eccentricity-Paced Monsoon Variability on the Northeastern Tibetan Plateau in the Late Oligocene High CO_2 World. *Sci. Adv.* **2021**, *7*, eabk2318. [CrossRef] [PubMed]
6. Pälike, H.; Norris, R.D.; Herrle, J.O.; Wilson, P.A.; Coxall, H.K.; Lear, C.H.; Shackleton, N.J.; Tripati, A.K.; Wade, B.S. The Heartbeat of the Oligocene Climate System. *Science* **2006**, *314*, 1894–1898. [CrossRef] [PubMed]
7. O'Brien, C.L.; Huber, M.; Thomas, E.; Pagani, M.; Super, J.R.; Elder, L.E.; Hull, P.M. The Enigma of Oligocene Climate and Global Surface Temperature Evolution. *Proc. Natl. Acad. Sci. USA* **2020**, *117*, 25302–25309. [CrossRef] [PubMed]
8. Gallagher, S.J.; Wade, B.; Li, Q.; Holdgate, G.R.; Bown, P.; Korasidis, V.A.; Scher, H.; Houben, A.J.; McGowran, B.; Allan, T. Eocene to Oligocene High Paleolatitude Neritic Record of Oi-1 Glaciation in the Otway Basin Southeast Australia. *Glob. Planet. Change* **2020**, *191*, 103218. [CrossRef]
9. Jin, C.-S.; Xu, D.; Li, M.; Hu, P.; Jiang, Z.; Liu, J.; Miao, Y.; Wu, F.; Liang, W.; Zhang, Q.; et al. Tectonic and Orbital Forcing of the South Asian Monsoon in Central Tibet during the Late Oligocene. *Proc. Natl. Acad. Sci. USA* **2023**, *120*, e2214558120. [CrossRef] [PubMed]
10. Yang, H.; Tang, W.; Xu, E.; Zhang, S.; Wang, Y.; Xu, M. Cyclostratigraphy and Paleoclimate Analysis of the Lingshui Formation in Changchang Sag, Qiongdongnan Basin, China. *Energy Geosci.* **2024**, *5*, 100224. [CrossRef]
11. Huang, C.; Hinnov, L. Astronomically Forced Climate Evolution in a Saline Lake Record of the Middle Eocene to Oligocene, Jianghan Basin, China. *Earth Planet. Sci. Lett.* **2019**, *528*, 115846. [CrossRef]
12. Wang, P.; Jian, Z.; Zhao, Q.; Li, Q.; Wang, R.; Liu, Z.; Wu, G.; Shao, L.; Wang, J.; Huang, B.; et al. Evolution of the South China Sea and Monsoon History Revealed in Deep-Sea Records. *Chin. Sci. Bull.* **2003**, *48*, 2549–2561. [CrossRef]
13. Gai, C.; Liu, Q.; Roberts, A.P.; Chou, Y.; Zhao, X.; Jiang, Z.; Liu, J. East Asian Monsoon Evolution since the Late Miocene from the South China Sea. *Earth Planet. Sci. Lett.* **2020**, *530*, 115960. [CrossRef]
14. Wang, P.; Li, Q. (Eds.) *The South China Sea: Paleoceanography and Sedimentology*; Developments in Paleoenvironmental Research; Springer: Dordrecht, The Netherlands, 2009. [CrossRef]
15. Clift, P.D.; Sun, Z. The Sedimentary and Tectonic Evolution of the Yinggehai–Song Hong Basin and the Southern Hainan Margin, South China Sea: Implications for Tibetan Uplift and Monsoon Intensification. *J. Geophys. Res. Solid Earth* **2006**, *111*, B06405. [CrossRef]
16. Wan, S.; Tian, J.; Steinke, S.; Li, A.; Li, T. Evolution and Variability of the East Asian Summer Monsoon during the Pliocene: Evidence from Clay Mineral Records of the South China Sea. *Palaeogeogr. Palaeoclimatol. Palaeoecol.* **2010**, *293*, 237–247. [CrossRef]
17. Wu, G.; Qin, J.; Mao, S. Deep-Water Oligocene Pollen Record from South China Sea. *Chin. Sci. Bull.* **2003**, *48*, 2511–2515. [CrossRef]
18. Xuan, C.; Li, Q.; Liu, C. Oligocene Biostratigraphy of Well W22 in the Liwan Sag of the Pearl River Mouth Basin. *Acta Micropalaeontol. Sin.* **2024**, *41*, 45–52.
19. Zhao, S.; Wang, Y.; Zhang, S.; Zhu, R.; Xu, E.; Yi, Z.; Gong, G.; Wang, Y.; Liu, H. Miocene Paleoclimate Analysis of the Northern South China Sea: Response to Cooling Events Based on Astronomical Cycles. *Mar. Geol. Front.* **2022**, *38*, 53–62.
20. Nie, Y.; Wu, H.; Satolli, S.; Ferré, E.C.; Shi, M.; Fang, Q.; Xu, Y.; Zhang, S.; Li, H.; Yang, T. Late Miocene to Present Paleoclimatic and Paleoenvironmental Evolution of the South China Sea Recorded in the Magneto-Cyclostratigraphy of IODP Site U1505. *Paleoceanogr. Paleoclimatol.* **2023**, *38*, e2022PA004547. [CrossRef]
21. He, P.; Zhang, S.; Xu, E.; Zhu, C. Milankovitch Cycles and the Astronomical Time Scale of the Zhujiang Formation in the Baiyun Sag, Pearl River Mouth Basin, China. *Open Geosci.* **2022**, *14*, 1380–1392. [CrossRef]
22. Zhu, C.; Zhang, S.; Wang, Y.; Xu, E. Cyclical Stratigraphic Analysis and Establishment of Astronomical Chronograph of Hanjiang Formation in Lufeng Sag. *Mar. Geol. Front.* **2022**, *38*, 42–52.
23. Zhang, S.; Xu, M.; Tang, W.; Xu, E.; Wang, Y.; Zhu, R. Cyclostratigraphy and Paleoclimate Analysis of the Lingshui Formation in the Beijiao Sag, Qiongdongnan Basin. *Bull. Geol. Sci. Technol.* **2025**, *44*, 95–105. [CrossRef]
24. Lin, X.; Shi, J.; Fan, J.; Ge, Z.; Gao, Z.; Fan, T.; Liu, Q.; Jin, Z. Astronomical Forcing–Driven Nonlinear Organic Carbon Burial and Lithofacies Evolution: Insights From Lacustrine Shale of the Funing Formation, Subei Basin, Eastern China. *Basin Res.* **2026**, *38*, e70137. [CrossRef]
25. Li, G.; Mei, L.; Ye, Q.; Pang, X.; Zheng, J.; Li, W. Post-Rift Faulting Controlled by Different Geodynamics in the Pearl River Mouth Basin, Northern South China Sea Margin. *Earth-Sci. Rev.* **2023**, *237*, 104311. [CrossRef]
26. Xu, C.; Gao, Y.; Liu, J.; Peng, G.; Qiu, X.; Zhang, X.; Jia, P. Major Discoveries and Significance of Hydrocarbon Exploration in the Paleogene Reservoirs of Panyu4 Subsag, Xijiang Sag, Pearl River Mouth Basin. *Acta Pet. Sin.* **2024**, *45*, 1031–1043. [CrossRef]

27. Xu, C.; Gao, Y.; Liu, J.; Peng, G.; Liu, P.; Xiong, W.; Song, P. Discovery and Inspiration of Large- and Medium-Sized Glutenite-Rich Oil and Gas Fields in the Eastern South China Sea: An Example from Paleogene Enping Formation in Huizhou 26 Subsag, Pearl River Mouth Basin. *Pet. Explor. Dev.* **2024**, *51*, 14–27. [CrossRef]
28. Tang, W.; Xie, X.; Xiong, L.; Guo, S.; Xu, M.; Xu, E.; Bai, H.; Liu, Z. Coupling Relationship and Genetic Mechanisms of Shelf-Edge Delta and Deep-Water Fan Source-to-Sink: A Case Study in Paleogene Zhuhai Formation in South Subsag of Baiyun Sag, Pearl River Mouth Basin, China. *Pet. Explor. Dev.* **2024**, *51*, 589–603. [CrossRef]
29. Zeng, Q.; Chen, G.; Zhang, G.; Ji, M.; Han, Y.; Guo, S.; Wang, L. The Shelf-Margin Delta Feature and Its Significance in Zhuhai Formation of Deep-Water Area, Pearl River Mouth Basin. *Acta Sedimentol. Sin.* **2015**, *33*, 595–606.
30. Ge, J.; Zhao, X.; Tan, M.; Zhuo, H.; Liu, C.; Jones, B.G. Sequence Stratigraphy and Depositional Evolution of the North-Eastern Shelf (33.9–10.5 Ma) of the Pearl River Mouth Basin, South China Sea. *Mar. Pet. Geol.* **2022**, *141*, 105697. [CrossRef]
31. Huang, C.; Ogg, J.G.; Kemp, D.B. Cyclostratigraphy and Astrochronology: Case Studies from China. *Palaeogeogr. Palaeoclim. Palaeoecol.* **2020**, *560*, 110017. [CrossRef] [PubMed]
32. Strasser, A.; Hilgen, F.J.; Heckel, P.H. Cyclostratigraphy—Concepts, Definitions, and Applications. *Newsl. Stratigr.* **2006**, *42*, 75–114. [CrossRef]
33. Li, M.; Huang, C.; Ogg, J.; Zhang, Y.; Hinnov, L.; Wu, H.; Chen, Z.-Q.; Zou, Z. Paleoclimate Proxies for Cyclostratigraphy: Comparative Analysis Using a Lower Triassic Marine Section in South China. *Earth-Sci. Rev.* **2019**, *189*, 125–146. [CrossRef]
34. Zeeden, C.; Ulfers, A.; Pierdominici, S.; Abadi, M.S.; Vinnepand, M.; Grelle, T.; Hesse, K.; Leu, K.; Wonik, T. Downhole Logging Data for Time Series Analysis and Cyclostratigraphy. *Earth-Sci. Rev.* **2023**, *241*, 104436. [CrossRef]
35. Peng, C.; Zou, C.; Zhang, S.; Shu, J.; Wang, C. Geophysical Logs as Proxies for Cyclostratigraphy: Sensitivity Evaluation, Proxy Selection, and Paleoclimatic Interpretation. *Earth-Sci. Rev.* **2024**, *252*, 104735. [CrossRef]
36. Li, Y.; Gong, C.; Qiu, X.; Qi, P.; He, Y.; Yu, Y. Source-to-Sink Processes and Their Controls on the Reservoirs of the Paleogene Huizhou Sag in Pearl River Mouth Basin. *Geol. Rev.* **2024**, *70*, 1403–1418.
37. Zhao, Q.; Wu, H.; Li, H.; Zhang, S. Determination of the Optimal Sampling Interval for Cyclostratigraphic Analysis by Using Sampling Theorem and Accumulation Rates. *Earth Sci.* **2011**, *36*, 12–16.
38. Wood, G.D.; Gabriel, A.M.; Lawson, J.C. Palynological Techniques—Processing and Microscopy. In *Palynology: Principles and Applications*; Jansonius, J., McGregor, D.C., Eds.; American Association of Stratigraphic Palynologists Foundation: Dallas, TX, USA, 1996; Volume 1, pp. 29–50.
39. Stockmarr, J. Tablets with Spores Used in Absolute Pollen Analysis. *Pollen Spores* **1971**, *13*, 615–621.
40. Neotoma Paleoecology Database. Tilia. Available online: https://www.neotomadb.org/apps/tilia (accessed on 23 October 2026).
41. Speijer, R.P.; Pälike, H.; Hollis, C.J.; Hooker, J.J.; Ogg, J.G. The Paleogene Period. In *Geologic Time Scale 2020*; Gradstein, F.M., Ogg, J.G., Schmitz, M.D., Ogg, G.M., Eds.; Elsevier: Amsterdam, The Netherlands, 2020; Volume 2, pp. 1087–1140. [CrossRef]
42. Raffi, I.; Wade, B.S.; Pälike, H.; Beu, A.; Cooper, R.; Crundwell, M.; Krijgsman, W.; Moore, T.; Raine, I.; Sardella, R.; et al. The Neogene Period. In *Geologic Time Scale 2020*; Gradstein, F.M., Ogg, J.G., Schmitz, M.D., Ogg, G.M., Eds.; Elsevier: Amsterdam, The Netherlands, 2020; Volume 2, pp. 1141–1215. [CrossRef]
43. Berggren, W.A.; Kent, D.V.; Swisher, C.C., III; Aubry, M.-P. A Revised Cenozoic Geochronology and Chronostratigraphy. In *Geochronology, Time Scales and Global Stratigraphic Correlation*; Berggren, W.A., Kent, D.V., Aubry, M.-P., Hardenbol, J., Eds.; Special Publication 54; SEPM Society for Sedimentary Geology: Tulsa, OK, USA, 1995; pp. 129–212. [CrossRef]
44. Li, Q.; Jian, Z.; Li, B. Oligocene–Miocene Planktonic Foraminifer Biostratigraphy, Site 1148, Northern South China Sea. In *Proceedings of the Ocean Drilling Program, Scientific Results*; Prell, W.L., Wang, P., Blum, P., Rea, D.K., Clemens, S.C., Eds.; Ocean Drilling Program: College Station, TX, USA, 2004; Volume 184, pp. 1–26. [CrossRef]
45. Bown, P.R.; Young, J.R. Techniques. In *Calcareous Nannofossil Biostratigraphy*; Bown, P.R., Ed.; Kluwer Academic Publishers: Dordrecht, The Netherlands, 1998; pp. 16–28.
46. Martini, E. Standard Tertiary and Quaternary Calcareous Nannoplankton Zonation. In *Proceedings of the Second Planktonic Conference*; Edizioni Tecnoscienza: Rome, Italy, 1971; pp. 739–785.
47. Okada, H.; Bukry, D. Supplementary modification and introduction of code numbers to the low-latitude coccolith biostratigraphic zonation (Bukry, 1973; 1975). *Mar. Micropaleontol.* **1980**, *5*, 321–325. [CrossRef]
48. Li, Q.; Lourens, L.; Wang, P. New Ages for Neogene Marine Biostratigraphic Events. *J. Stratigr.* **2007**, *31*, 197–208.
49. Okada, H. Calcareous Nannofossils from Deep Sea Drilling Project Sites 442 through 446, Philippine Sea. *Init. Rep. Deep Sea Drill. Proj.* **1980**, *58*, 549–565.
50. Cohen, K.M.; Harper, D.A.T.; Gibbard, P.L.; Car, N. The ICS International Chronostratigraphic Chart This Decade. *Episodes* **2025**, *48*, 105–115. [CrossRef] [PubMed]
51. Li, M.; Hinnov, L.; Kump, L. Acycle: Time-Series Analysis Software for Paleoclimate Research and Education. *Comput. Geosci.* **2019**, *127*, 12–22. [CrossRef]

52. Li, M.; Kump, L.R.; Hinnov, L.A.; Mann, M.E. Tracking Variable Sedimentation Rates and Astronomical Forcing in Phanerozoic Paleoclimate Proxy Series with Evolutionary Correlation Coefficients and Hypothesis Testing. *Earth Planet. Sci. Lett.* **2018**, *501*, 165–179. [CrossRef]
53. Laskar, J.; Robutel, P.; Joutel, F.; Gastineau, M.; Correia, A.C.M.; Levrard, B. A Long-Term Numerical Solution for the Insolation Quantities of the Earth. *Astron. Astrophys.* **2004**, *428*, 261–285. [CrossRef]
54. Larsen, H.C.; Jian, Z.; Alvarez Zarikian, C.A.; Sun, Z.; Stock, J.M.; Klaus, A.; Boaga, J.; Bowden, S.A.; Briais, A.; Chen, Y.; et al. Site U1501. In *South China Sea Rifted Margin. Proceedings of the International Ocean Discovery Program*; International Ocean Discovery Program: College Station, TX, USA, 2018; Volume 367/368.
55. Mao, S.; Li, J.; Qin, X.; Wu, G.; Harland, R. Dinoflagellate Cysts and Environmental Evolution of the Oligocene to Lower Miocene at Site 1148, ODP Leg 184, South China Sea. *Palynology* **2007**, *31*, 37–52. [CrossRef]
56. Miao, Y.; Wu, F.; Herrmann, M.; Yan, X.; Meng, Q. Late Early Oligocene East Asian Summer Monsoon in the NE Tibetan Plateau: Evidence from a Palynological Record from the Lanzhou Basin, China. *J. Asian Earth Sci.* **2013**, *75*, 46–57. [CrossRef]
57. Chalabe, A.C.; Olivera, D.E.; Martínez, M.A.; Zavala, C. Palaeoenvironments and Palaeoclimate of the Uppermost Cuyo Group and Lowermost Lotena Group at Quebrada Álvarez, Picún Leufú Sub-Basin, Patagonia, Argentina: A Preliminary Study Based on Palynology. *Palynology* **2024**, *48*, 2254364. [CrossRef]
58. Juggins, S.; Birks, H.J.B. Quantitative Environmental Reconstructions from Biological Data. In *Tracking Environmental Change Using Lake Sediments: Data Handling and Numerical Techniques*; Birks, H.J.B., Lotter, A.F., Juggins, S., Smol, J.P., Eds.; Springer: Dordrecht, The Netherlands, 2012; Volume 5, pp. 431–494. [CrossRef]
59. Sanchez Botero, C.A.; Oboh-Ikuenobe, F.E.; Grabel, L.; Adojoh, O.C. Palynomorphs in Southern Western Australian Lake Sediments: Evidence of Climate Change and Hypersalinity during the Cenozoic. *Palynology* **2021**, *45*, 201–214. [CrossRef]
60. Obigba, S.O. Understanding Past and Present Vegetation Dynamics Using the Palynological Approach: An Introductory Discourse. In *Vegetation Index and Dynamics*; IntechOpen: London, UK, 2022; p. 221.
61. Viganò, A.; Dallanave, E.; Alegret, L.; Westerhold, T.; Sutherland, R.; Dickens, G.R.; Newsam, C.; Agnini, C. Calcareous Nannofossils and Paleoclimatic Evolution across the Eocene-Oligocene Transition at IODP Site U1509, Tasman Sea, Southwest Pacific Ocean. *Paleoceanogr. Paleoclimatol.* **2024**, *39*, e2023PA004738. [CrossRef]
62. Béjard, T.M.; Rigual-Hernández, A.S.; Flores, J.A.; Tarruella, J.P.; de Madron, X.D.; Cacho, I.; Haghipour, N.; Hunter, A.; Sierro, F.J. Calcification Response of Planktic Foraminifera to Environmental Change in the Western Mediterranean Sea during the Industrial Era. *Biogeosciences* **2023**, *20*, 1505–1528. [CrossRef]
63. Bown, P.R. (Ed.) *Calcareous Nannofossil Biostratigraphy*; British Micropalaeontological Society Publications Series; Chapman & Hall: London, UK, 1998.
64. Roth, P.H.; Thierstein, H.R. Calcareous Nannoplankton: Leg 14 of the Deep Sea Drilling Project. *Init. Rep. Deep Sea Drill. Proj.* **1972**, *14*, 421–485. [CrossRef]
65. Imbrie, J.; Kipp, N.G. A New Micropaleontological Method for Quantitative Paleoclimatology: Application to a Late Pleistocene Caribbean Core. In *The Late Cenozoic Glacial Ages*; Turekian, K.K., Ed.; Yale University Press: New Haven, CT, USA, 1971; pp. 71–181.
66. Kucera, M. Planktonic Foraminifera as Tracers of Past Oceanic Environments. In *Proxies in Late Cenozoic Paleoceanography*; Hillaire-Marcel, C., de Vernal, A., Eds.; Developments in Marine Geology; Elsevier: Amsterdam, The Netherlands, 2007; Volume 1, pp. 213–262. [CrossRef]
67. Li, J.; Hu, X.; Zachos, J.C.; Garzanti, E.; BouDagher-Fadel, M. Sea Level, Biotic and Carbon-Isotope Response to the Paleocene–Eocene Thermal Maximum in Tibetan Himalayan Platform Carbonates. *Glob. Planet. Change* **2020**, *194*, 103316. [CrossRef]
68. Edgar, K.M.; Pälike, H.; Wilson, P.A. Testing the Impact of Diagenesis on the $\delta^{18}O$ and $\delta^{13}C$ of Benthic Foraminiferal Calcite from a Sediment Burial Depth Transect in the Equatorial Pacific. *Paleoceanography* **2013**, *28*, 468–480. [CrossRef]
69. Fischer, G.; Wefer, G. (Eds.) *Use of Proxies in Paleoceanography: Examples from the South Atlantic*; Springer Science & Business Media: Berlin/Heidelberg, Germany, 1999. [CrossRef]
70. Wang, P.; Suo, Y.; Peng, G.; Li, S.; Du, X.; Cao, X.; Zhou, J.; Wang, G.; Santosh, M.; Jiang, S.; et al. Three-Stage Extension in the Cenozoic Pearl River Mouth Basin Triggering Onset of the South China Sea Spreading. *Gondwana Res.* **2023**, *120*, 31–46. [CrossRef]
71. Laskar, J.; Fienga, A.; Gastineau, M.; Manche, H. La2010: A New Orbital Solution for the Long-Term Motion of the Earth. *Astron. Astrophys.* **2011**, *532*, A89. [CrossRef]
72. Laepple, T.; Lohmann, G. Seasonal Cycle as Template for Climate Variability on Astronomical Timescales. *Paleoceanography* **2009**, *24*, PA4201. [CrossRef]
73. Zhang, J.; Wang, C.; Teng, X.; Kemp, D.B.; Wang, Z.; Yang, H.; Gai, C.; Zhang, Y.; Zhong, Y.; Jiang, X.; et al. Orbital Modulation of an Intensified Hydrological Cycle during the Paleocene-Eocene Thermal Maximum. *Earth Planet. Sci. Lett.* **2024**, *635*, 118693. [CrossRef]
74. Zhang, R.; Huang, C.; Kemp, D.B.; Wang, Z.; Zhang, Z.; Chen, W. Astronomical Forcing of the Hydrological Cycle in the Weihe Basin (North China) during the Middle to Late Eocene. *Glob. Planet. Change* **2023**, *228*, 104208. [CrossRef]

75. Ziegler, M.; Tuenter, E.; Lourens, L.J. The Precession Phase of the Boreal Summer Monsoon as Viewed from the Eastern Mediterranean (ODP Site 968). *Quat. Sci. Rev.* **2010**, *29*, 1481–1490. [CrossRef]
76. Naish, T.; Powell, R.; Levy, R.; Wilson, G.; Scherer, R.; Talarico, F.; Krissek, L.; Niessen, F.; Pompilio, M.; Wilson, T.; et al. Obliquity-Paced Pliocene West Antarctic Ice Sheet Oscillations. *Nature* **2009**, *458*, 322–328. [CrossRef] [PubMed]
77. Liebrand, D.; de Bakker, A.T.M.; Beddow, H.M.; Wilson, P.A.; Bohaty, S.M.; Ruessink, G.; Pälike, H.; Batenburg, S.J.; Hilgen, F.J.; Hodell, D.A.; et al. Evolution of the Early Antarctic Ice Ages. *Proc. Natl. Acad. Sci. USA* **2017**, *114*, 3867–3872. [CrossRef] [PubMed]
78. Li, T.; Liu, F.; Abels, H.A.; You, C.-F.; Zhang, Z.; Chen, J.; Ji, J.; Li, L.; Li, L.; Liu, H.-C.; et al. Continued Obliquity Pacing of East Asian Summer Precipitation after the Mid-Pleistocene Transition. *Earth Planet. Sci. Lett.* **2017**, *457*, 181–190. [CrossRef]
79. Bosmans, J.H.C.; Hilgen, F.J.; Tuenter, E.; Lourens, L.J. Obliquity Forcing of Low-Latitude Climate. *Clim. Past* **2015**, *11*, 1335–1346. [CrossRef]
80. Zhang, Z.; Licht, A.; De Vleeschouwer, D.; Wang, Z.; Li, Y.; Kemp, D.B.; Tan, L.; Zhang, R.; Qiang, X.; Huang, C. East Asian Monsoonal Climate Sensitivity Changed in the Late Pliocene in Response to Northern Hemisphere Glaciations. *Geophys. Res. Lett.* **2022**, *49*, e2022GL101280. [CrossRef]
81. Lü, L.; Fang, X.; Mason, J.A.; Li, J.; An, Z. The Evolution of Coupling of Asian Winter Monsoon and High Latitude Climate of Northern Hemisphere: Grain Evidence from 8.1 Ma Loess-Red Clay Sequence on the Chinese Central Loess Plateau. *Sci. China Ser. D Earth Sci.* **2001**, *44*, 185–191. [CrossRef]
82. Liebrand, D.; Lourens, L.J.; Hodell, D.A.; de Boer, B.; van de Wal, R.S.W.; Pälike, H. Antarctic Ice Sheet and Oceanographic Response to Eccentricity Forcing during the Early Miocene. *Clim. Past* **2011**, *7*, 869–880. [CrossRef]
83. Cramer, B.S.; Toggweiler, J.R.; Wright, J.D.; Katz, M.E.; Miller, K.G. Ocean Overturning since the Late Cretaceous: Inferences from a New Benthic Foraminiferal Isotope Compilation. *Paleoceanography* **2009**, *24*, PA4216. [CrossRef]
84. Li, M.; Hinnov, L.A.; Huang, C.; Ogg, J.G. Sedimentary Noise and Sea Levels Linked to Land–Ocean Water Exchange and Obliquity Forcing. *Nat. Commun.* **2018**, *9*, 1004. [CrossRef] [PubMed]
85. Dunbar, G.B.; Naish, T.R.; Barrett, P.J.; Fielding, C.; Powell, R. Constraining the Amplitude of Late Oligocene Bathymetric Changes in Western Ross Sea during Orbitally-Induced Oscillations in the East Antarctic Ice Sheet: (1) Implications for Glacimarine Sequence Stratigraphic Models. *Palaeogeogr. Palaeoclimatol. Palaeoecol.* **2008**, *260*, 50–65. [CrossRef]
86. Zhong, X.C.; Zhao, C.B.; Yang, S.Z.; Shen, H.; Xu, K.; Liang, H.D.; Fu, Z.Y.; XU, D.Y.; Wang, R.; Chen, J.P. *Jurassic System in the North of China, Volume II: Palaeoenvironment and Oil-Gas Source*; Petroleum Industry Press: Beijing, China, 2003.
87. Guitián, J.; Fuertes, M.Á.; Flores, J.-A.; Hernández-Almeida, I.; Stoll, H. Variation in Calcification of Reticulofenestra Coccoliths over the Oligocene–Early Miocene. *Biogeosciences* **2022**, *19*, 5007–5019. [CrossRef]
88. Ma, R.; Aubry, M.-P.; Bord, D.; Jin, X.; Liu, C. Inferred Nutrient Forcing on the Late Middle Eocene to Early Oligocene (~ 40–31 Ma) Evolution of the Coccolithophore Reticulofenestra (Order Isochrysidales). *Paleobiology* **2024**, *50*, 29–42. [CrossRef]
89. Broecker, W.S.; Peng, T.-H. *Tracers in the Sea*; Lamont-Doherty Geological Observatory, Columbia University: Palisades, NY, USA, 1982.
90. Archer, D.E. Equatorial Pacific Calcite Preservation Cycles: Production or Dissolution? *Paleoceanography* **1991**, *6*, 561–571. [CrossRef]
91. Westerhold, T.; Marwan, N.; Drury, A.J.; Liebrand, D.; Agnini, C.; Anagnostou, E.; Barnet, J.S.K.; Bohaty, S.M.; De Vleeschouwer, D.; Florindo, F.; et al. An Astronomically Dated Record of Earth's Climate and Its Predictability over the Last 66 Million Years. *Science* **2020**, *369*, 1383–1387. [CrossRef] [PubMed]
92. Hyeong, K.; Lee, J.; Seo, I.; Lee, M.J.; Yoo, C.M.; Khim, B.-K. Southward Shift of the Intertropical Convergence Zone due to Northern Hemisphere Cooling at the Oligocene-Miocene Boundary. *Geology* **2014**, *42*, 667–670. [CrossRef]
93. Beddow, H.M.; Liebrand, D.; Wilson, D.S.; Hilgen, F.J.; Sluijs, A.; Wade, B.S.; Lourens, L.J. Astronomical Tunings of the Oligocene–Miocene Transition from Pacific Ocean Site U1334 and Implications for the Carbon Cycle. *Clim. Past* **2018**, *14*, 255–270. [CrossRef]
94. Ogg, J.G. Geomagnetic Polarity Time Scale. In *Geologic Time Scale 2020*; Gradstein, F.M., Ogg, J.G., Schmitz, M.D., Ogg, G.M., Eds.; Elsevier: Amsterdam, The Netherlands, 2020; Volume 1, pp. 159–192. [CrossRef]

Disclaimer/Publisher's Note: The statements, opinions and data contained in all publications are solely those of the individual author(s) and contributor(s) and not of MDPI and/or the editor(s). MDPI and/or the editor(s) disclaim responsibility for any injury to people or property resulting from any ideas, methods, instructions or products referred to in the content.